SCIENTIFIC REPORTS

OPEN

Chronic disturbance in the thalamus following cranial irradiation to the developing mouse brain

Received: 11 March 2019
Accepted: 18 June 2019
Published online: 03 July 2019

Martina Boström[1,2], Yohanna Eriksson[1], Jolie Danial[1], Thomas Björk-Eriksson[2] & Marie Kalm[1]

Better survival rates among pediatric brain tumor patients have resulted in an increased awareness of late side effects that commonly appear following cancer treatment. Radiation-induced changes in hippocampus and white matter are well described, but do not explain the full range of neurological late effects in childhood cancer survivors. The aim of this study was to investigate thalamus following cranial irradiation (CIR) to the developing brain. At postnatal day 14, male mice pups received a single dose of 8 Gy CIR. Cellular effects in thalamus were assessed using immunohistochemistry 4 months after CIR. Interestingly, the density of neurons decreased with 35% ($p = 0.0431$) and the density of astrocytes increased with 44% ($p = 0.011$). To investigate thalamic astrocytes, S100β$^+$ cells were isolated by fluorescence-activated cell sorting and genetically profiled using next-generation sequencing. The phenotypical characterization indicated a disrupted function, such as downregulated microtubules' function, higher metabolic activity, immature phenotype and degraded ECM. The current study provides novel insight into that thalamus, just like hippocampus and white matter, is severely affected by CIR. This knowledge is of importance to understand the late effects seen in pediatric brain tumor survivors and can be used to give them the best suitable care.

Better survival rates among pediatric brain tumor patients have resulted in an increased awareness of the late side effects that can appear following cancer treatment. The treatment strategies used to cure a child from a brain tumor consist of surgery, chemotherapy and radiotherapy. It is well known that radiotherapy towards the brain can cause lifelong late effects, such as impairments in processing speed, working memory, executive function and attention[1,2]. Further, it has been shown that even low doses of ionizing radiation to the brain can cause intellectual impairment as well as perturbed growth and puberty[3]. The mechanisms of chronic radiation damage have been proposed to be related to long-term toxicity of oligodendrocytes, endothelial cells and normal neural cell types, including stem and progenitor cells, in combination with metabolic derangements, glial reactions, and inflammatory responses[2,4]. Most research have focused on radiation-induced changes in the hippocampus and white matter[1,5], but injuries in those brain regions do not explain the full range of all neurological late effects seen in childhood cancer survivors.

Cranial radiotherapy during childhood has been coupled with altered sleep-wake rhythm in adulthood[6]. A brain region important for this control is the thalamus[7,8]. However, the role of the thalamus in pediatric brain tumor survivors remains to be clarified. The thalamus is located between the cortex and the midbrain with direct connectivity to many subcortical structures, and was formerly believed to be merely a passive central sensory and motor relay station. Today, there is evidence implicating that the thalamus is contributing directly to cognitive functions as diverse as memory, attention, perception, motor planning, language processing, motivation, decision-making, and the monitoring of self-generated actions[7]. At the same time, the specific mechanisms by which the thalamus shapes these cognitions and behaviors remain unknown. Due to thalamus' role in functions that are greatly affected by cranial radiotherapy (e.g. sleep/wakefulness and cognition), and the lack of

[1]Department of Pharmacology, Institute of Neuroscience and Physiology at the Sahlgrenska Academy, University of Gothenburg, Gothenburg, Sweden. [2]Department of Oncology, Institute of Clinical Sciences at the Sahlgrenska Academy, University of Gothenburg, Gothenburg, Sweden. Martina Boström and Yohanna Eriksson contributed equally. Correspondence and requests for materials should be addressed to M.K. (email: marie.kalm@gu.se)

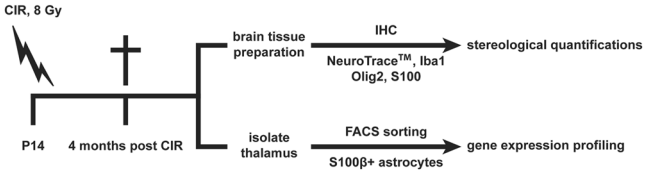

Figure 1. An overview of the study outline. At postnatal day 14 (P14), the animals were subjected to a single dose of 8 Gy cranial irradiation (CIR). The animals were sacrificed 4 months later. One group of animals was used for immunohistochemistry (IHC) to quantify neurons (NeuroTrace™), Iba1$^+$ microglia, Olig2$^+$ oligodendrocytes and S100$^+$ astrocytes in the thalamus. Another group of animals was used to isolate S100β$^+$ thalamic astrocytes using fluorescence-activated cell sorting (FACS) and perform gene expression profiling using next-generation sequencing (NGS).

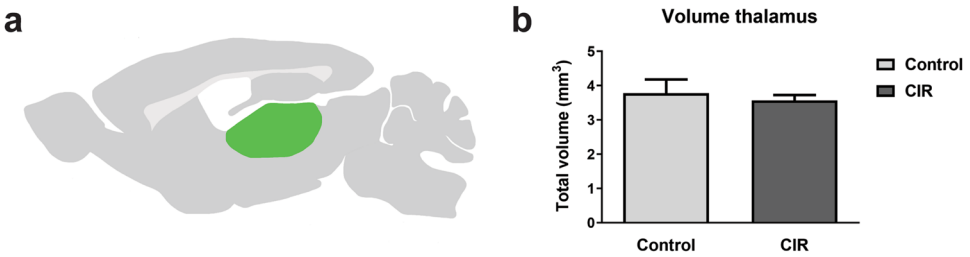

Figure 2. Volume measurement of the thalamus. An illustration of the location of the thalamus (green) in the mouse brain is shown in (**a**). The volume of the thalamus was measured 4 months following CIR (**b**). Data shown as mean ± SEM. CIR = cranial irradiation, n = 10–11 per group.

research performed within the area, it poses a highly interesting brain region to investigate further following cranial radiotherapy.

The aim of this study was to investigate chronic alterations in the thalamus 4 months following cranial irradiation (CIR) to the young mouse brain. Cellular effects in the thalamus was first assessed by stereological quantifications of neurons, microglia, oligodendrocytes and astrocytes. These analyses revealed a decreased density of neurons and an increased density of astrocytes in the thalamus following CIR. To further unravel the role of this increased proportion of astrocytes, S100 calcium-binding protein (S100β)$^+$ astrocytes were isolated from the thalamus by fluorescence-activated cell sorting (FACS) and genetically profiled using next-generation sequencing (NGS). This phenotypical characterization indicated that thalamic astrocytes are affected by CIR with a disrupted function, such as downregulated microtubules' function, higher metabolic activity, immature phenotype and degraded ECM. This study provides novel insight into that the thalamus, just like the hippocampus and white matter, is severely affected by CIR.

Results

Cellular composition in the thalamus following CIR. In the current study, postnatal day 14 (P14) mice were subjected to a single dose of 8 Gy CIR and sacrificed 4 months later. The study outline is illustrated in Fig. 1. Cellular composition in the thalamus following CIR was examined by stereological quantifications (thoroughly described in the method section).

Volume. We have previously observed a smaller volume in both the hippocampus and the corpus callosum following CIR[9,10]. Therefore, the volume was measured to assess the CIR-induced injury in the thalamus. However, the thalamic volume was not affected by CIR in the current study (Fig. 2b).

Neurons. Cellular effects in the thalamus was further assessed by quantifying mature neurons (NeuroTrace™). Interestingly, the density of thalamic neurons was reduced with 35% in irradiated animals compared to controls ($p = 0.0431$, Fig. 3a).

Microglia. To further evaluate non-neuronal cells we quantified ionized calcium-binding adapter molecule 1 (Iba1)$^+$ microglia in the thalamus. Microglia are known to play a key function in the inflammatory response in the brain and loss of these cells have previously been shown in the juvenile brain following CIR[11]. However, their response in the thalamus has remained unexplored. The thalamic microglia were unchanged 4 months following CIR-induced injury to the developing brain (Fig. 3b).

Oligodendrocytes. We have previously observed a radiation-induced reduction of oligodendrocytes in the hippocampus (12 days following CIR) and in the corpus callosum (4 months following CIR)[9,10]. Considering the important function in generating myelin sheets to facilitate neuronal signaling within the central nervous system (CNS), we decided to quantify oligodendrocyte transcription factor 2 (Olig2)$^+$ oligodendrocytes in the thalamus.

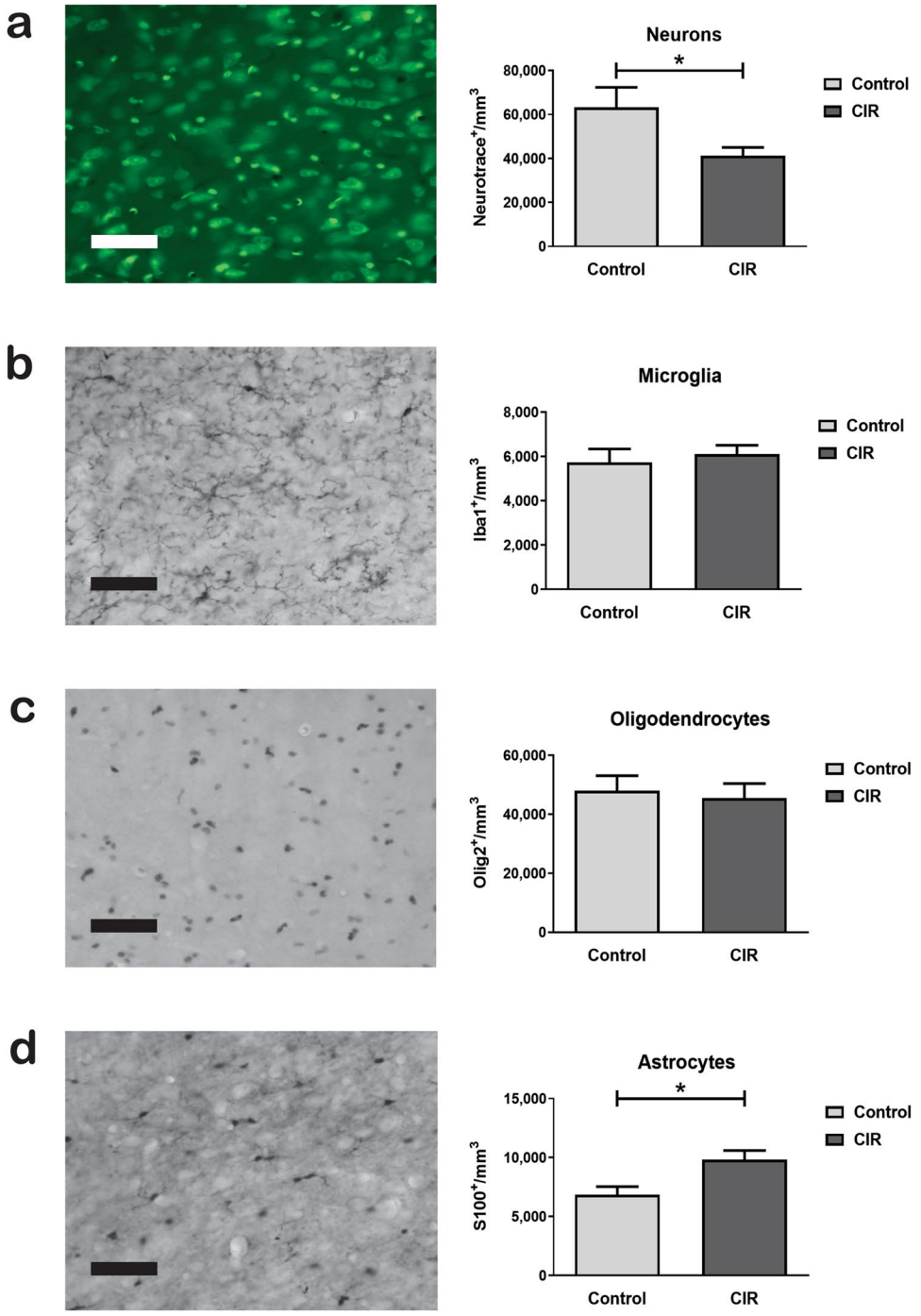

Figure 3. Cellular effects in the thalamus following CIR. Cellular quantifications were performed using a stereological approach in the thalamus 4 months following CIR at P14. A representative microphotograph and the density of mature neurons (NeuroTrace™) (**a**), Iba1$^+$ microglia (**b**), Olig2$^+$ oligodendrocytes (**c**), and S100$^+$ astrocytes (**d**) are shown. *$p < 0.05$. Data shown as mean ± SEM. CIR = Cranial irradiation, P14 = postnatal day 14, n = 9–11 per group. Scale bar = 50 µm.

However, in contrast to the hippocampus and the corpus callosum, no difference was observed in the density of oligodendrocytes 4 months after CIR in the thalamus (Fig. 3c).

Astrocytes. Astrocytes are another non-neuronal cell population that have a key role in the healthy brain, but also following an injury. We have previously observed effects on astrocytes in the hippocampus as long as one year following CIR[12]. In the current study, we performed stereological quantifications of S100$^+$ astrocytes (possibly including a subpopulation of neurons). Interestingly, the density of astrocytes was increased by 44% ($p = 0.011$, Fig. 3d). This was a particularly interesting finding considering that the opposite effect was seen in the density of neurons.

Gene expression in astrocytes following CIR. To further unravel the role of thalamic astrocytes in radiation-induced injury, we chose to isolate S100β$^+$ astrocytes by FACS (Fig. 4A–C) and phenotypically characterize those using NGS. The flow cytometry analysis showed an increased amount of astrocytes by 54% in CIR-treated animals compared to controls ($p < 0.001$, Fig. 4D), similar to the stereologically assessed quantification (44% increase). Further, the NGS analysis showed a CIR-induced transcriptome change in thalamic astrocytes. Of the significantly altered genes, 57 were up-regulated and 155 were down-regulated after CIR (Supplementary Table 1). Genes that were found to be annotated or predicted genes on GeneCards® (https://www.genecards.org/), were further evaluated on PubMed. Those described in the literature, and that were related to the following irradiation-induced injury mechanism: injury response; proliferation, differentiation and survival; extracellular matrix; intracellular crosstalk, morphogenesis and motility, are described in more detail below (Figs 5–8).

Fourteen injury-related genes were affected following CIR (Fig. 5), where eight were downregulated and six were upregulated. The thalamic astrocytes are presumably set to a healing state, with activated clearance mechanisms and lower levels of inflammation, as indicated by increased levels of *Nov*, *Gpnmb, Ces2f* and *Ephx1*[13–16]. However, some genes (*Bank1, Il1a*, and *Pdgfra*) indicate that there is still an ongoing injury present as long as 4 months following CIR[17–19].

Among the genes that were related to proliferation, differentiation and survival, 12 genes were downregulated and seven were upregulated (Fig. 6). The increased expression of *Ceacam2* suggests a higher metabolic activity in astrocytes following CIR[20]. This could possibly be explained by the increased expression of genes involved in proliferation, e.g. *Cks2*[21]. Further, genes related to astrocytic development (*Inha* and *Bmp5*) indicate an immature phenotype[22,23]. In line with this, the astrocytes attempt to restore the lack of neurons as indicated by increased levels of *Neurod1*, which has been shown to be able to convert astrocytes to neurons[24]. In general, genes involved in synaptic plasticity and behavior, propose that the astrocytes are trying to restore the CIR-induced dysfunction (*Sfrp4, Plekha2, Nxph1*)[25–27].

Following prophylactic radiotherapy to the brain, lower levels of extracellular matrix (ECM) proteins in the cerebrospinal fluid from adult small cell lung cancer patients have previously been shown[28]. In line with this, all genes related to ECM showed reduced expression in the current study, indicating a degradation of the ECM following CIR (Fig. 7). This could play an important part in the healing process following CIR, since the ECM function as a barrier for plasticity and axon regeneration.

Among the genes that were related to intracellular crosstalk, morphogenesis and motility, 24 genes were downregulated and one was upregulated following CIR (Fig. 8). Genes important for microtubules' function were all downregulated (*Stmn1*, *Tppp3, Dnah2*, *Dnah3*, *Dnah6*, *Dnah10*, *Dnah11*, *Dnah12, Gas2l1* and *Gas2l2*)[29–31]. Further, genes involved in actin reorganization and stabilization were all downregulated (*Tpm2, Iqgap2*)[32,33]. However, *Kif5a*, connected to transport of cellular organelles and proteins[34] was upregulated. Taken together, the gene expression following CIR indicates a disturbed astrocytic phenotype in the thalamus.

Discussion

The survival rate for pediatric brain tumor patients has improved significantly and advancements in the health care will most likely lead to a continuously increasing number of survivors in the society, living with treatment-induced side effects that could have a negative impact on their quality of life. In this study, we wanted to increase the knowledge regarding the lifelong late effects seen following cranial radiotherapy to the developing brain with focus on the thalamus. The main findings from this study were the following: 1) The density of neurons were decreased in the thalamus after CIR. 2) The amount of astrocytes were increased in the thalamus following CIR. 3) The phenotype of the astrocytes are affected by CIR, with alterations such as downregulated microtubules' function, higher metabolic activity, immature phenotype and degraded ECM, indicating a disrupted function. 4) The volume of the thalamus was not altered by CIR to the developing brain. This knowledge adds another piece to the puzzle in the complexity behind brain regions that are affected by cranial radiotherapy.

In this study the density of neurons in the thalamus was decreased, whereas the density of astrocytes was increased. This cellular disturbance most likely interferes with the normal function of the thalamus. A similar cellular effect following cranial radiation has been shown in the hippocampus, where inflammation has been suggested as the driving force in making precursor cells become astrocytes instead of neurons[35]. Interestingly, the thalamus display similar alterations as the hippocampus except for the lack of growth previously seen in the hippocampus[36,37], and no effects on oligodendrocytes and microglia. In the hippocampus, both microglia and oligodendrocytes are decreased following irradiation to the young mouse brain[10,11]. This is an interesting difference between the brain regions, which could possibly be explained by that the thalamus at the time of CIR (P14) is more mature compared to the hippocampus, making the thalamus less vulnerable. For example, the mediodorsal thalamus in rodents has its growth peak before P13[38] whereas hippocampus is still growing at the time of CIR[36,37]. Differences between brain regions following CIR have previously been shown in a study where the subventricular zone recovered with time but the hippocampus did not[39]. In our previous studies of white matter and the hippocampus, a decrease of oligodendrocytes was observed[9,10]. The current study show a different response with unaltered density of oligodendrocytes but less neurons in the thalamus, indicating that the oligodendrocytes have less axons to myelinate. Oligodendrocytes are known to be able to myelinate several axons simultaneously[40]. This study is the first to report these observed cellular disturbances in the thalamus following CIR-induced damage.

The increased density of astrocytes was shown using two different methods (immunohistochemistry and FACS), thereby strengthening the validity of the data. It has previously been shown that quantification of cell populations using flow cytometry correlate well with quantitative immunohistochemistry[41]. Our NGS results from the FACS isolated astrocytes indicate that the astrocytes are trying to restore the CIR-induced

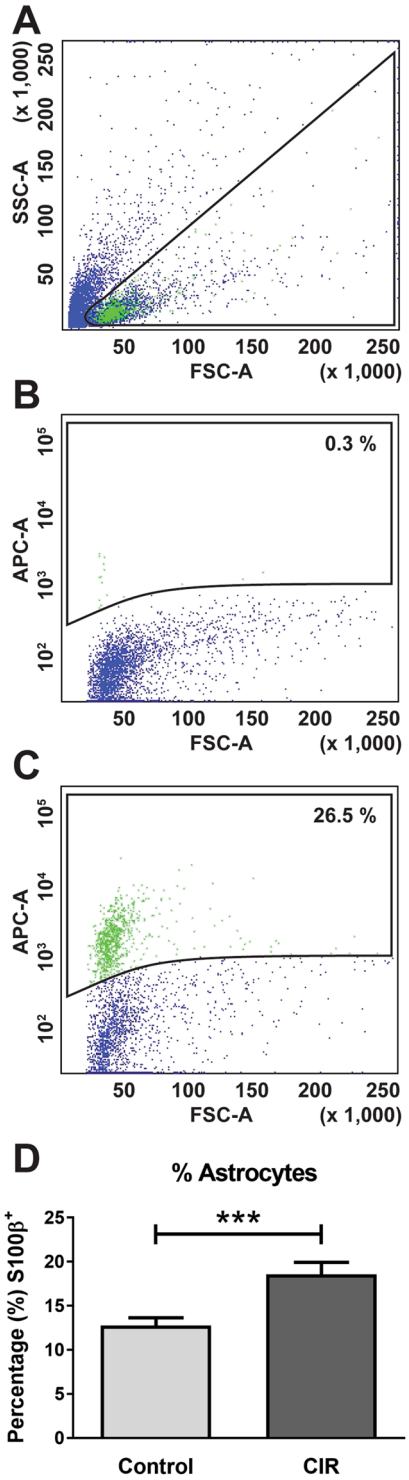

Figure 4. FACS analysis of S100β$^+$ astrocytes in the brain following CIR. Gating strategy for sorting of S100β$^+$ astrocytes from the thalamus. (**A**) shows the SSC vs FSC plot which was used to gate cells from debris, (**B**) shows a negative control staining where the primary antibody was omitted and the (**C**) panel shows a representative sample stained with S100β. (**D**) show quantification of the relative numbers (%) of S100β$^+$ astrocytes within the entire heterogeneous cell population analyzed by flow cytometry during the isolation of astrocytes with FACS. ***$p < 0.001$. Data shown as mean ± SEM. CIR = Cranial irradiation, FACS = fluorescence-activated cell sorting, FSC = forward scatter, SSC = side scatter, $n_{control} = 20$ and $n_{irradiated} = 12$.

dysfunction (*Sfrp4, Plekha2, Nxph1*)[25–27] and even try to convert into neurons (*Neurod1*)[24] (Fig. 6). For example, *Sfrp4*, known to inhibit the Wnt pathway that controls cell proliferation, differentiation and migration, was downregulated following CIR[25]. The gene expression data do however also indicate that there is

	Fold Change	Gene		log2FoldChange	p-value	Reference
Injury response	0.513	Trbc1	T cell receptor beta constant region 1	-0.963	0.039	Andres-Benito P, Moreno J, Dominguez R, Aso E, Povedano M, Ferrer I. Inflammatory Gene Expression in Whole Peripheral Blood at Early Stages of Sporadic Amyotrophic Lateral Sclerosis. Frontiers in neurology 2017, 8: 546.
	0.551	Nov	nephroblastoma overexpressed gene	-0.860	0.002	Jones EV, Bouvier DS. Astrocyte-secreted matricellular proteins in CNS remodelling during development and disease. Neural plasticity 2014, 2014: 321209.
	0.568	Ly6d	lymphocyte antigen 6 complex locus D	-0.817	0.025	Inlay MA, Bhattacharya D, Sahoo D, Serwold T, Seita J, Karsunky H, et al. Ly6d marks the earliest stage of B-cell specification and identifies the branchpoint between B-cell and T-cell development. Genes & development 2009, 23(20): 2376-2381.
	0.629	Tnfsf4	tumor necrosis factor (ligand) superfamily member 4	-0.670	0.021	Yashiro T, Hara M, Ogawa H, Okumura K, Nishiyama C. Critical Role of Transcription Factor PU.1 in the Function of the OX40L/TNFSF4 Promoter in Dendritic Cells. Scientific reports 2016, 6: 34825.
	0.639	Il1f8	interleukin 1 family member 8	-0.647	0.048	Penha R, Higgins J, Mutamba S, Barrow P, Mahida Y, Foster N. IL-36 receptor is expressed by human blood and intestinal T lymphocytes and is dose-dependently activated via IL-36beta and induces CD4+ lymphocyte proliferation. Cytokine 2016, 85: 18-25.
	0.761	Aebp1	AE binding protein 1	-0.394	0.044	Shijo, M., H. Honda, S. O. Suzuki, H. Hamasaki, M. Hokama, N. Abolhassani, Y. Nakabeppu, T. Ninomiya, T. Kitazono and T. Iwaki (2018). "Association of adipocyte enhancer-binding protein 1 with Alzheimer's disease pathology in human hippocampi." Brain Pathol **28**(1): 58-71.
	0.789	Cytip	cytohesin 1 interacting protein	-0.343	0.038	Hofer S, Pfeil K, Niederegger H, Ebner S, Nguyen VA, Kremmer E, et al. Dendritic cells regulate T-cell deattachment through the integrin-interacting protein CYTIP. Blood 2006, 107(3): 1003-1009.
	0.795	Bank1	B cell scaffold protein with ankyrin repeats 1	-0.331	0.037	Yang J, Ren J, Yang Y, Sun J, Zhou X, Zheng S, et al. BANK1 alters B cell responses and influences the interactions between B cells and induced T regulatory cells in mice with collagen-induced arthritis. Arthritis research & therapy 2018, 20(1): 9.
	1.303	Gpnmb	glycoprotein (transmembrane) nmb	0.382	0.036	Neal ML, Boyle AM, Budge KM, Safadi FF, Richardson JR. The glycoprotein GPNMB attenuates astrocyte inflammatory responses through the CD44 receptor. J Neuroinflammation 2018, 15(1): 73.
	1.317	Pdgfra	platelet derived growth factor receptor alpha polypeptide	0.398	0.038	Shijo M, Honda H, Suzuki SO, Hamasaki H, Hokama M, Abolhassani N, et al. Association of adipocyte enhancer-binding protein 1 with Alzheimer's disease pathology in human hippocampi. Brain pathology (Zurich, Switzerland) 2018, 28(1): 58-71.
	1.341	Ephx1	epoxide hydrolase 1 microsomal	0.423	0.010	Anderson GD, Peterson TC, Vonder Haar C, Farin FM, Bammler TK, MacDonald JW, et al. Effect of Traumatic Brain Injury, Erythropoietin, and Anakinra on Hepatic Metabolizing Enzymes and Transporters in an Experimental Rat Model. The AAPS journal 2015, 17(5): 1255-1267.
	1.421	Il1a	interleukin 1 alpha	0.507	0.036	Dinarello CA. Immunological and inflammatory functions of the interleukin-1 family. Annual review of immunology 2009, 27: 519-550.
	1.515	Ces2f	carboxylesterase 2F	0.600	0.024	Zhao M, Zhang T, Yu F, Guo L, Wu B. E4bp4 regulates carboxylesterase 2 enzymes through repression of the nuclear receptor Rev-erbalpha in mice. Biochemical pharmacology 2018, 152: 293-301.
	2.561	Trav12-1	T cell receptor alpha variable 12-1	1.357	0.037	Mitchell AM, Kaiser Y, Falta MT, Munson DJ, Landry LG, Eklund A, et al. Shared alphabeta TCR Usage in Lungs of Sarcoidosis Patients with Lofgren's Syndrome. Journal of immunology (Baltimore, Md : 1950) 2017, 199(7): 2279-2290.

Figure 5. Gene alterations related to injury-responses in thalamic astrocytes following CIR. Significantly altered genes are shown. Genes were evaluated on PubMed and the most relevant reference were added. Data are presented as relative gene expression compared to controls in log2 scale. CIR = cranial irradiation.

an ongoing injury (*Bank1, Il1a*, and *Pdgfra*)[17–19] (Fig. 5), and all genes related to ECM were downregulated (Fig. 7). To illustrate, *Il1a*, a proinflammatory cytokine with costimulatory effects of different T lymphocyte functions, was increased following CIR by 42%[18]. However, it should be noted that the vast down-regulated gene expression observed in thalamic astrocytes in the current study (57 were up-regulated and 155 were down-regulated after CIR), could be a consequence of the increased numbers of thalamic astrocytes in irradiated animals. In this study, an increased expression of *Ceacam2* (Fig. 6) was observed, suggesting a higher metabolic activity in thalamic astrocytes following CIR[20]. This finding is supported by a study of adult male macaque monkeys which showed increased glucose metabolism in the thalamus following a total dose of 40 Gy fractionated whole-brain irradiation (fWBI)[42]. Together, these results indicate that as long as 4 months following CIR to the young brain there are still ongoing processes related to the CIR-induced injury. It remains to determine which of these processes that poses a target of interest to restore normal brain function following CIR. The results from the astrocytic gene expression analysis should however be interpreted with precaution as many of the genes have previously not been associated with or shown to be expressed by astrocytes. Another aspect to keep in mind is that type of radiation, dose rate, and single or fractionated dosing could affect the radiobiological response. For example, a study performed on adult rats propose that the cellular response following a single dose of cranial irradiation does not predict the cellular response following biological equivalent fractioned radiation doses[43]. Further, it has been shown that the molecular response to fractionated irradiation is slower compared to single dose irradiation[44,45]. It is also important to note that the adult and the juvenile brain respond significantly different to cranial irradiation, at least in the hippocampus[46]. In summary, the data presented in the present study provide novel insight into the unexplored function of astrocytes in the thalamus, both in naïve and irradiated animals.

Late effects following cranial radiotherapy in childhood, such as altered sleep-wake rhythm and problems with memory and attention, could all be linked to the thalamus due to the diverse role of this brain region[6–8]. In this study, we did not observe any change in volume of the thalamus after CIR, which could explain why the thalamus has not been studied in greater detail following radiotherapy towards the brain. For example, both white matter and the hippocampus are known to display smaller volumes following cranial radiotherapy and both, especially the hippocampus, are well described in the literature[1,9,10,47–49]. However, the volumetric results from the thalamus in the current study are supported by a previous study from our group, as well as a study of children with acute lymphoblastic leukemia that also showed no change in thalamic volume following cranial radiotherapy[10,50]. Regarding cellular alterations in the thalamus following cranial radiotherapy, one study has shown reduced gray matter density in the thalamus after prophylactic cranial irradiation to adult small cell lung cancer patients[51]. Moreover, another study showed higher apparent diffusion coefficient (ADC) values, measured by diffusion tensor imaging (DTI), in the thalamus of children with medulloblastoma treated with craniospinal radiation compared to controls[52]. An increased ADC indicate that there are more free water in the tissue following radiation, which is of particular interest since the NGS data from the current study point towards a degraded ECM. More water in the tissue could also explain the reduced gray matter density from the Simo *et al.* study. Further, Mabbot *et al.*, showed that decreased fractional anisotropy (FA) and increased ADC were related to lower intellectual outcome in patients relative to age-matched controls[52]. In another study, FA values were significantly reduced in normal appearing cerebral white matter of the temporal lobe, hippocampus, and thalamus in adult survivors treated with fWBI for acute lymphoblastic leukemia[53,54]. The correlation between compromised fiber integrity, tissue loss, and lower IQ is consistent with findings in previous studies that show that white matter volume loss

	Fold Change	Gene		log2FoldChange	p-value	Reference
Proliferation, differentiation and survival	0.661	Sfrp4	secreted frizzled-related protein 4	-0.597	0.026	Zhang Y, Zhang M, Li L, Wei B, He A, Lu L, et al. Methylation-reprogrammed Wnt/beta-catenin signalling mediated prenatal hypoxia-induced brain injury in foetal and offspring rats. Journal of cellular and molecular medicine 2018.
	0.678	Inha	inhibin alpha	-0.560	0.045	Fujimura H, Ohsawa K, Funaba M, Murata T, Murata E, Takahashi M, et al. Immunological localization and ontogenetic development of inhibin alpha subunit in rat brain. J Neuroendocrinol 1999, 11(3): 157-163.
	0.692	Bmp5	bone morphogenetic protein 5	-0.532	0.030	Brederlau A, Faigle R, Kaplan P, Odin P, Funa K. Bone morphogenetic proteins but not growth differentiation factors induce dopaminergic differentiation in mesencephalic precursors. Mol Cell Neurosci 2002, 21(3): 367-378.
	0.695	Igfbp6	insulin-like growth factor binding protein 6	-0.525	0.036	Barkho BZ, Song H, Aimone JB, Smrt RD, Kuwabara T, Nakashima K, et al. Identification of astrocyte-expressed factors that modulate neural stem/progenitor cell differentiation. Stem cells and development 2006, 15(3): 407-421.
	0.701	Igfbp4	insulin-like growth factor binding protein 4	-0.513	0.024	Chesik D, De Keyser J, Glazenburg L, Wilczak N. Insulin-like growth factor binding proteins: regulation in chronic active plaques in multiple sclerosis and functional analysis of glial cells. Eur J Neurosci 2006, 24(6): 1645-1652.
	0.725	Cdr1	cerebellar degeneration related antigen 1	-0.465	0.015	Barbagallo D, Condorelli A, Ragusa M, Salito L, Sammito M, Banelli B, et al. Dysregulated miR-671-5p / CDR1-AS / CDR1 / VSNL1 axis is involved in glioblastoma multiforme. Oncotarget 2016, 7(4): 4746-4759.
	0.736	Dthd1	death domain containing 1	-0.442	0.028	Wang C, Li L, Yin Z, Zhang Q, Zhao H, Tao R, *et al.* An indel polymorphism within pre-miR3131 confers risk for hepatocellular carcinoma. *Carcinogenesis* 2017, **38**(2): 168-176.
	0.743	Adamts20	a disintegrin-like and metallopeptidase (reprolysin type) with thrombospondin type 1 motif 20	-0.428	0.013	Wang YH, Liou KT, Tsai KC, Liu HK, Yang LM, Chern CM, et al. GSK-3 inhibition through GLP-1R allosteric activation mediates the neurogenesis promoting effect of P7C3 after cerebral ischemic/reperfusional injury in mice. Toxicology and applied pharmacology 2018, 357: 88-105.
	0.760	Ppan	peter pan homolog	-0.396	0.024	Pfister AS, Keil M, Kuhl M. The Wnt Target Protein Peter Pan Defines a Novel p53-independent Nucleolar Stress-Response Pathway. *J Biol Chem* 2015, **290**(17): 10905-10918.
	0.777	Ddr2	discoidin domain receptor family member 2	-0.364	0.007	Hebron M, Peyton M, Liu X, Gao X, Wang R, Lonskaya I, et al. Discoidin domain receptor inhibition reduces neuropathology and attenuates inflammation in neurodegeneration models. J Neuroimmunol 2017, 311: 1-9.
	0.793	Grm7	glutamate receptor metabotropic 7	-0.336	0.024	Xia W, Liu Y, Jiao J. GRM7 regulates embryonic neurogenesis via CREB and YAP. Stem cell reports 2015, 4(5): 795-810.
	0.801	Plekha2	pleckstrin homology domain-containing family A (phosphoinositide binding specific) member 2	-0.320	0.050	Li H, Hou S, Wu X, Nandagopal S, Lin F, Kung S, et al. The tandem PH domain-containing protein 2 (TAPP2) regulates chemokine-induced cytoskeletal reorganization and malignant B cell migration. PLoS One 2013, 8(2): e57809.
	1.232	Shisa7	shisa family member 7	0.301	0.047	Schmitz LJM, Klaassen RV, Ruiperez-Alonso M, Zamri AE, Stroeder J, Rao-Ruiz P, et al. The AMPA receptor-associated protein Shisa7 regulates hippocampal synaptic function and contextual memory. eLife 2017, 6.
	1.300	Nxph1	neurexophilin 1	0.379	0.021	Neupert C, Schneider R, Klatt O, Reissner C, Repetto D, Biermann B, et al. Regulated Dynamic Trafficking of Neurexins Inside and Outside of Synaptic Terminals. J Neurosci 2015, 35(40): 13629-13647.
	1.314	Ceacam2	carcinoembryonic antigen-related cell adhesion molecule 2	0.394	0.025	Patel PR, Ramakrishnan SK, Kaw MK, Raphael CK, Ghosh S, Marino JS, et al. Increased metabolic rate and insulin sensitivity in male mice lacking the carcino-embryonic antigen-related cell adhesion molecule 2. Diabetologia 2012, 55(3): 763-772.
	1.423	Gria3	glutamate receptor ionotropic	0.509	0.000	Beyer B, Deleuze C, Letts VA, Mahaffey CL, Boumil RM, Lew TA, et al. Absence seizures in C3H/HeJ and knockout mice caused by mutation of the AMPA receptor subunit Gria4. Human molecular genetics 2008, 17(12): 1738-1749.
	1.450	Grin3b	glutamate receptor ionotropic	0.536	0.012	Niemann S, Kanki H, Fukui Y, Takao K, Fukaya M, Hynynen MN, et al. Genetic ablation of NMDA receptor subunit NR3B in mouse reveals motoneuronal and nonmotoneuronal phenotypes. Eur J Neurosci 2007, 26(6): 1407-1420.
	1.625	Neurod1	neurogenic differentiation 1	0.701	0.015	Zhang L, Yin JC, Yeh H, Ma NX, Lee G, Chen XA, et al. Small Molecules Efficiently Reprogram Human Astroglial Cells into Functional Neurons. Cell Stem Cell 2015, 17(6): 735-747.
	1.655	Cks2	CDC28 protein kinase regulatory subunit 2	0.727	0.042	Yu MH, Luo Y, Qin SL, Wang ZS, Mu YF, Zhong M. Up-regulated CKS2 promotes tumor progression and predicts a poor prognosis in human colorectal cancer. American journal of cancer research 2015, 5(9): 2708-2718.

Figure 6. Gene alterations related to proliferation, differentiation, and survival in thalamic astrocytes following CIR. Significantly altered genes are shown. Genes were evaluated on PubMed and the most relevant reference were added. Data are presented as relative gene expression compared to controls in log2 scale. CIR = cranial irradiation.

	Fold Change	Gene		log2FoldChange	p-value	Reference
Extracellular matrix	0.448	Cma2	chymase 2 mast cell	-1.159	0.004	Arsene D, Vasilescu F, Toader C, Balan A, Popa C, Ardeleanu C. Clinico-pathological correlations in fatal ischemic stroke. An immunohistochemical study of human brain penumbra. *Romanian journal of morphology and embryology = Revue roumaine de morphologie et embryologie* 2011, **52**(1): 29-38.
	0.626	Dcn	decorin	-0.675	0.011	Reviewed in Frey H, Schroeder N, Manon-Jensen T, Iozzo RV, Schaefer L. Biological interplay between proteoglycans and their innate immune receptors in inflammation. The
	0.629	Lum	lumican	-0.668	0.037	
	0.680	Efemp1	epidermal growth factor-containing fibulin-like extracellular matrix protein 1	-0.557	0.008	Nandhu MS, Behera P, Bhaskaran V, Longo SL, Barrera-Arenas LM, Sengupta S, et al. Development of a Function-Blocking Antibody Against Fibulin-3 as a Targeted Reagent for Glioblastoma. Clin Cancer Res 2018, 24(4): 821-833.
	0.695	Col8a2	collagen type VIII, alpha 2	-0.525	0.001	Reviewed in Pawelec KM, Best SM, Cameron RE. Collagen: a network for regenerative medicine. Journal of materials chemistry B 2016, 4(40): 6484-6496.
	0.701	Emb	embigin	-0.512	0.022	Guenette RS, Sridhar S, Herley M, Moolbroek M, Wong P, Tenniswood M. Embigin, a developmentally expressed member of the immunoglobulin super family, is also expressed during regression of prostate and mammary gland. Developmental genetics 1997, 21(4): 268-278.
	0.714	Mrc2	mannose receptor C type 2	-0.486	0.014	Madsen DH, Ingvarsen S, Jurgensen HJ, Melander MC, Kjoller L, Moyer A, et al. The non-phagocytic route of collagen uptake: a distinct degradation pathway. J Biol Chem 2011, 286(30): 26996-27010.
	0.725	Thbs1	thrombospondin 1	-0.465	0.008	Garcia O, Torres M, Helguera P, Coskun P, Busciglio J. A role for thrombospondin-1 deficits in astrocyte-mediated spine and synaptic pathology in Down's syndrome. PLoS One 2010, 5(12): e14200.
	0.729	Col6a2	collagen type VI, alpha 2	-0.456	0.008	Reviewed in Pawelec KM, Best SM, Cameron RE. Collagen: a network for regenerative medicine. Journal of materials chemistry B 2016, 4(40): 6484-6496.
	0.737	Bgn	biglycan	-0.440	0.035	Reviewed in Frey H, Schroeder N, Manon-Jensen T, Iozzo RV, Schaefer L. Biological interplay between proteoglycans and their innate immune receptors in inflammation. The FEBS journal 2013, 280(10): 2165-2179.
	0.784	Col1a1	collagen type I, alpha 1	-0.352	0.016	Reviewed in Pawelec KM, Best SM, Cameron RE. Collagen: a network for regenerative medicine. Journal of materials chemistry B 2016, 4(40): 6484-6496.
	0.804	Col11a2	collagen type XI, alpha 2	-0.315	0.043	
	0.828	Col12a1	collagen type XII, alpha 1	-0.273	0.034	

Figure 7. Gene alterations related to extracellular matrix in thalamic astrocytes following CIR. Significantly altered genes are shown. Genes were evaluated on PubMed and the most relevant reference were added. Data are presented as relative gene expression compared to controls in log2 scale. CIR = cranial irradiation.

is related to adverse intelligence and academic outcome[55,56]. Our findings shed light on why the clinical DTI data from the thalamus are altered following cranial radiotherapy, and show that the thalamus can be added to the list of affected regions in the brain following cranial radiotherapy.

The current study revealed an increased density of astrocytes and decreased density of neurons, a disturbance that is most likely contributing to the late effects seen in pediatric brain tumor survivors. These results now need to be verified further in humans and the question of how to restore the thalamus still remains. Several studies have used pharmacological interventions and physical exercise following CIR to the developing brain and investigated effects in for example the hippocampus[10,57,58]. It would now be of great interest to see if any of them also have positive effects in the thalamus following CIR-induced damage. The new knowledge presented in the current study is of importance to understand the late effects seen in pediatric brain tumor survivors and can be used in the future to give them the best suitable habilitation.

	Fold Change	Gene		log2FoldChange	p-value	Reference
Intracellular crosstalk, morphogenesis and motility	0.573	Sspo	SCO-spondin	-0.804	0.014	Grondona JM, Hoyo-Becerra C, Visser R, Fernandez-Llebrez P, Lopez-Avalos MD. The subcommissural organ and the development of the posterior commissure. International review of cell and molecular biology 2012, 296: 63-137.
	0.682	Caly	calcyon neuron-specific vesicular protein	-0.553	0.028	Shi L, Muthusamy N, Smith D, Bergson C. Dynein binds and stimulates axonal motility of the endosome adaptor and NEEP21 family member, calcyon. The international journal of biochemistry & cell biology 2017, 90: 93-102.
	0.703	Tpm2	tropomyosin 2 beta	-0.508	0.039	Had L, Faivre-Sarrailh C, Legrand C, Rabie A. The expression of tropomyosin genes in pure cultures of rat rorns, astrocytes and oligodendrocytes is highly cell-type specific and strongly regulated during development. Brain research Molecular brain research 1993, 18(1-2): 77-86.
	0.717	Gas2l2	growth arrest-specific 2 like 2	-0.480	0.026	Stroud MJ, Nazgiewicz A, McKenzie EA, Wang Y, Kammerer RA, Ballestrem C. GAS2-like proteins mediate communication between microtubules and actin through interactions with end-binding proteins. Journal of cell science 2014, 127(Pt 12): 2672-2682.
	0.721	Tppp3	tubulin polymerization-promoting protein family member 3	-0.472	0.019	Huang R, Chen M, Yang L, Wagle M, Guo S, Hu B. MicroRNA-133b Negatively Regulates Zebrafish Single Mauthner-Cell Axon Regeneration through Targeting tppp3 in Vivo. Frontiers in molecular neuroscience 2017, 10: 375.
	0.732	Stmn1	stathmin 1	-0.450	0.035	Yamada K, Matsuzaki S, Hattori T, Kuwahara R, Taniguchi M, Hashimoto H, et al. Increased stathmin1 expression in the dentate gyrus of mice causes abnormal axonal arborizations. PLoS One 2010, 5(1): e8596.
	0.755	Dnah6	dynein axonemal heavy chain 6	-0.405	0.019	Reviewed in Roberts AJ, Kon T, Knight PJ, Sutoh K, Burgess SA. Functions and mechanics of dynein motor proteins. Nature reviews Molecular cell biology 2013, 14(11): 713-726.
	0.761	Cfap52	cilia and flagella associated protein 52	-0.395	0.048	Reviewed in Knowles MR, Daniels LA, Davis SD, Zariwala MA, Leigh MW. Primary ciliary dyskinesia. Recent advances in diagnostics, genetics, and characterization of clinical disease. American journal of respiratory and critical care medicine 2013, 188(8): 913-922
	0.770	Foxj1	forkhead box J1	-0.377	0.048	Jacquet BV, Salinas-Mondragon R, Liang H, Therit B, Buie JD, Dykstra M, et al. FoxJ1-dependent gene expression is required for differentiation of radial glia into ependymal cells and a subset of astrocytes in the postnatal brain. Development (Cambridge, England) 2009, 136(23): 4021-4031.
	0.772	Cfap44	cilia and flagella associated protein 44	-0.373	0.008	Reviewed in Knowles MR, Daniels LA, Davis SD, Zariwala MA, Leigh MW. Primary ciliary dyskinesia. Recent advances in diagnostics, genetics, and characterization of clinical disease. American journal of respiratory and critical care medicine 2013, 188(8): 913-922
	0.777	Dnah12	dynein axonemal heavy chain 12	-0.365	0.016	Reviewed in Roberts AJ, Kon T, Knight PJ, Sutoh K, Burgess SA. Functions and mechanics
	0.779	Dnah3	dynein axonemal heavy chain 3	-0.360	0.011	of dynein motor proteins. Nature reviews Molecular cell biology 2013, 14(11): 713-726.
	0.784	Rilpl2	Rab interacting lysosomal protein-like 2	-0.351	0.040	Lise MF, Srivastava DP, Arstikaitis P, Lett RL, Sheta R, Viswanathan V, et al. Myosin-Va-interacting protein, RILPL2, controls cell shape and neuronal morphogenesis via Rac signaling. Journal of cell science 2009, 122(Pt 20): 3810-3821.
	0.786	Gas2l1	growth arrest-specific 2 like 1	-0.348	0.043	Stroud MJ, Nazgiewicz A, McKenzie EA, Wang Y, Kammerer RA, Ballestrem C. GAS2-like proteins mediate communication between microtubules and actin through interactions with end-binding proteins. Journal of cell science 2014, 127(Pt 12): 2672-2682.
	0.786	Dnah10	dynein axonemal heavy chain 10	-0.348	0.016	Reviewed in Roberts AJ, Kon T, Knight PJ, Sutoh K, Burgess SA. Functions and mechanics of dynein motor proteins. Nature reviews Molecular cell biology 2013, 14(11): 713-726.
	0.791	Hydin	HYDIN axonemal central pair apparatus protein	-0.338	0.025	Lechtreck KF, Delmotte P, Robinson ML, Sanderson MJ, Witman GB. Mutations in Hydin impair ciliary motility in mice. J Cell Biol 2008, 180(3): 633-643.
	0.792	Iqgap2	IQ motif containing GTPase activating protein 2	-0.337	0.016	Schmidt VA, Scudder L, Devoe CE, Bernards A, Cupit LD, Bahou WF. IQGAP2 functions as a GTP-dependent effector protein in thrombin-induced platelet cytoskeletal reorganization. Blood 2003, 101(8): 3021-3028.
	0.797	Cep126	centrosomal protein 126	-0.328	0.031	Bonavita R, Walas D, Brown AK, Luini A, Stephens DJ, Colanzi A. Cep126 is required for pericentriolar satellite localisation to the centrosome and for primary cilium formation. Biology of the cell 2014, 106(8): 254-267.
	0.806	Dnah2	dynein axonemal heavy chain 2	-0.312	0.015	Reviewed in Roberts AJ, Kon T, Knight PJ, Sutoh K, Burgess SA. Functions and mechanics
	0.808	Dnah11	dynein axonemal heavy chain 11	-0.308	0.038	of dynein motor proteins. Nature reviews Molecular cell biology 2013, 14(11): 713-726.
	0.819	Cfap43	cilia and flagella associated protein 43	-0.287	0.043	Reviewed in Knowles MR, Daniels LA, Davis SD, Zariwala MA, Leigh MW. Primary ciliary dyskinesia. Recent advances in diagnostics, genetics, and characterization of clinical disease. American journal of respiratory and critical care medicine 2013, 188(8): 913-922
	0.820	Dcdc5	doublecortin domain containing 5	-0.287	0.041	Kaplan A, Reiner O. Linking cytoplasmic dynein and transport of Rab8 vesicles to the midbody during cytokinesis by the doublecortin domain-containing 5 protein. Journal of cell science 2011, 124(Pt 23): 3989-4000.
	0.821	Cfap54	cilia and flagella associated protein 54	-0.284	0.041	Reviewed in Knowles MR, Daniels LA, Davis SD, Zariwala MA, Leigh MW. Primary ciliary
	0.830	Cfap61	cilia and flagella associated protein 61	-0.269	0.049	dyskinesia. Recent advances in diagnostics, genetics, and characterization of clinical
	1.308	Kif5a	kinesin family member 5A	0.388	0.018	Hares K, Miners JS, Cook AJ, Rice C, Scolding N, Love S, et al. Overexpression of Kinesin Superfamily Motor Proteins in Alzheimer's Disease. Journal of Alzheimer's disease : JAD 2017, 60(4): 1511-1524.

Figure 8. Gene alterations related to intracellular crosstalk, morphogenesis and motility following CIR. Significantly altered genes are shown. Genes were evaluated on PubMed and the most relevant reference were added. Data are presented as relative gene expression compared to controls in log2 scale. CIR = cranial irradiation.

Materials and Methods

Animals. Male C57BL/6J mice were purchased from Charles River Breeding Laboratories (Sulzfeld, Germany. Animals were housed according to normal procedures at the Experimental Biomedicine animal facility (University of Gothenburg, Gothenburg, Sweden). The mice were kept on a 12-h light cycle with food and water provided *ad libitum*. The room temperature was 19–21 °C with 40–70% relative humidity. All experiments were approved by the Swedish Animal Welfare Agency (application no. 2015–72). Further, all experiments were performed in accordance with relevant guidelines and regulations.

Irradiation procedure. A linear accelerator (Varian Clinac 1600 C-2 (250 Mu/min, 2.4 Gy/min) and True Beam STX (600 Mu/min, 5.6 Gy/min), Radiation Oncology Systems, LLC, San Diego, CA, USA) with 6 MV nominal photon energy were used to irradiate mice on P14. The mice were anesthetized with an intraperitoneal (i.p.) injection of tribromoethanol (Sigma, Stockholm, Sweden), placed on a polystyrene bed in prone position (head to gantry) and irradiated with a symmetrical 2×2 cm radiation field. A tissue equivalent material covered the head to obtain an even radiation dose distribution in the underlying tissue. The source to skin distance was approximately 99.5 cm and the irradiated tissue received a single absorbed dose of 8 Gy with a dose variation of $\pm 5\%$. Using the LQ model[59] and an alpha/beta ratio of 3 for late effects in the normal brain tissue, the acute exposure of 8 Gy is equivalent to approximately 18 Gy when delivered in repeated 2 Gy fractions. Animals were kept on a warm bed (36 °C) both before and after CIR to maintain body temperature. Control animals were anesthetized but did not receive any CIR.

Cellular composition in the thalamus following CIR. *Tissue preparation.* Animals were deeply anesthetized with sodium pentobarbital (Pentothal, Electra-box Pharma, Tyresö, Sweden) before being transcardially perfused with a 6% formaldehyde solution buffered with sodium phosphate at pH 7.4 and stabilized with methanol (Histofix; Histolab products AB, Gothenburg, Sweden). The brains were immersion-fixed in Histofix for 24 h after perfusion and then changed to 30% sucrose solution containing 100 mM phosphate buffer, pH 7.5. After equilibration in sucrose, the brains were fixed with a cryo-gel (Tissue-Tec® O.C.T. compound, Sakura® Finetek, Alphen aan den Rijn, The Netherlands) to a dry ice-cooled copper block and one hemisphere was sagitally cut into 25 μm sections with a sliding microtome (Leica SM2000R, Leica Microsystems, Nussloch, Germany). Serial sections were collected in a series of 12 tubes containing tissue cryoprotectant solution (TCS; 25% ethylene glycol, 25% glycerine and 0.05 M phosphate buffer), and stored at 4 °C until used for immunohistochemistry.

NeuroTrace™ Fluorescent Nissl stain. Sections were rinsed in TBS and then washed in TBS with 0.1% Triton X-100 for 10 min. After further washing, sections were incubated with NeuroTrace™ 500/525Green Fluorescent Nissl stain for 20 min (N21480, ThermoFisher Scientific, USA). Following several rinsing steps in TBS, the sections were mounted and cover slipped with ProLong® Gold Antifade Reagent (Thermo-Fisher Scientific, USA).

Immunohistochemistry for Iba1, Olig2 and S100. Stainings for stereological analysis were performed on every 12th section and rinsed in Tris-buffered saline (TBS; 0.08 mol/L Trizma-HCl, 0.016 mol/L Trizma-Base, 0.15 mol/L NaCl, pH 7.5) before staining. After rinsing in TBS, sections underwent two subsequent steps to avoid unspecific binding. First, endogenous peroxidase activity was blocked by incubating the sections in 30% hydrogen peroxide (H_2O_2) for 30 min, followed by rinsing in TBS. This was followed by 30 min incubation in TBS with 3% donkey serum and 0.1% Triton X-100 (blocking solution) to avoid unspecific antigen binding. Sections were incubated at 4 °C overnight with primary antibodies against Iba1 (rabbit anti-Iba1, 1:1000, Wako Pure Chemical Industries Ltd. Osaka, Japan), Olig2 (goat anti-Olig2, 1:1000, R&D Systems, Minneapolis, MN,USA) or S100 (rabbit anti-S100, 1:5000, Dako Cytomation, Glostrup, Denmark), diluted in blocking solution. The following day, the sections were rinsed and a biotinylated secondary antibody was added for 1 h at room temperature (donkey anti-rabbit IgG, 1:1000, or donkey anti-goat IgG, 1:1000, all from Jackson Immunoresearch Laboratories Inc). This was followed by rinsing and amplification with avidin-biotin enzyme complex (ABC kit, Vectastain Elite, Vector Laboratories, Burlingame, CA, USA) for 1 hour. Finally, sections were once again rinsed and staining was developed using 0.25 mg/mL 3–30-diaminobenzindine tetrahydrochloride (DAB, Saveen Werner AB, Malmö, Sweden) diluted in TBS containing 0.009% H_2O_2 and 0.04% nickel chloride to enhance the reaction. Omission of the primary antibodies yielded only very weak nonspecific staining, and the identification of the immunopositive cells was facilitated by their characteristic morphology and location.

Stereological procedures. Cells were counted in every 12th section using systematic-random sampling (Stereoinvestigator, MicroBrightField, USA) and a Leica DM6000 B microscope (Leica Microsystems, Germany) at 20x magnification. Counting started on sections containing a clearly separated/divided dorsal and ventral hippocampus. The thalamic area was traced at either 5x or 10x magnification. Total volumes were calculated according to the Cavalieri principle, using the following formula: $V = SA \times P \times T$, where V is the total volume, SA is the sum of area measurements, P is the inverse of the sampling fraction and T is the section thickness. For Iba1, all immunopositive cells in the thalamus were counted. The total number of Iba1$^+$ cells was obtained by multiplying the number of counted cells with the series fraction (1/12), and the density acquired by dividing the total number of Iba1$^+$ cells with the volume.

For neurons (NeuroTrace™ staining), Olig2$^+$ and S100$^+$ cells, a grid (500 × 500-μm for NeuroTrace™, 375 × 375-μm for Olig2 and 300 × 300-μm for S100) was randomly placed over the thalamic traced area and counting frames (100 × 100-μm for NeuroTrace™ and Olig2, and 150 × 150-μm for S100) were placed within the grid. The total number of cells per animal was calculated by dividing the number of counted cells with the sampling fractions, i.e., fraction of sampling area/total traced area × series fraction (1/12) × optical dissector height/physical section thickness. Finally, the density was calculated by dividing the total number of cells with the volume.

Next generation sequencing of isolated astrocytes. *Isolation of cells from tissue.* Mice were deeply anesthetized with sodium pentobarbital (Pentothal®; Electra-box Pharma, Tyresö, Sweden) and decapitated 4 months after CIR. Brains were rapidly removed from the cranium, followed by rinsing in sterile 0.9% NaCl. The thalamus was collected by microdissection and transferred into gentleMACS C Tubes (Milentyi Biotec, Bergisch Gladbach, Germany) containing 2 mL of ice cold papain/protease/DNase I enzyme solution consisting of 0.01% papain (Worthington, Lakewood, NJ, USA), 0.1% Dispase II (SigmaAldrich, Saint Louis, MO, USA), 0.01% DNase I (Worthington, Lakewood, NJ, USA) and 12.4 mM $MgSO_4$ diluted in HBSS without Ca^{2+} and Mg^{2+} (Hank's Balanced Salt Solution; Worthington, Lakewood, NJ, USA). The left and right thalamus from the same animal were placed in a tube as one single sample and further processed together according to Milentyi Biotec´s adult brain dissociation kit for mice and rat (with significant modification), in order to obtain a single cell suspension devoid of connective tissue.

GentleMACS C tubes were tightly closed and attached upside down onto the sleeve of the gentleMACS Octo Dissociator. The gentleMACS **m_brain_01** program was run, followed by 15 min incubation on low rotation at 37 °C. This was followed by running the **m_brain_02** program, 10 min incubation on low rotation at 37 °C, running the **m_brain_03** program and finally 10 min incubation on low rotation at 37 °C. The C tubes were thereafter centrifuged briefly to collect the sample at the bottom of the tube. Samples were triturated ~15 times (in about 30 s) with a cotton plugged 9 inch pasteur pipette with the tip barely fire polished to an opening of 0.7–1.1 mm D (inferior) (ORIGIO, Målov, Denmark), followed by 10 min incubation at 37 °C. After incubation, tissue pieces were once again gently triturated ~15 times, followed by 10 min incubation at 37 °C and finally gently triturated ~15 times until no pieces were visible.

MACS SmartStrainers (70 μm) were placed on 15 mL Falcon tubes and washed with ~10 mL of cold (4 °C) Dulbecco´s Phosphate-buffered Saline (D-PBS; Gibco/Invitrogen, San Diego, CA, USA). The fluid was discarded. Resuspended samples were applied to the MACS SmartStrainer, followed by rinsing the C tubes with 5 mL cold (4 °C) D-PBS and transferring the fluid onto the MACS SmartStrainers. An additional 5 mL cold (4 °C) D-PBS was then applied onto the MACS SmartStrainers before they were discarded. Cell suspensions in the 15 mL Falcon tubes were centrifuged at 100 × g for 10 min at 4 °C and supernatant were aspirated completely. The cell suspensions were resuspended in 1 mL of D-PBS and transferred to 2 mL Eppendorf tubes.

Debris removal. A volume of 300 µL cold Debris Removal Solution (Milentyi Biotec, Bergisch Gladbach, Germany) were added to the cell suspension and mixed thoroughly. The mixed solution was gently overlaid with ~700 µL cold D-PBS, making sure that the phases were not mixed. After 10 min centrifugation at 200 × g at 4 °C, three phases were formed, and the two upper phases were completely aspirated and discarded. The tubes were filled up with cold D-PBS to a final volume of 2 mL and gently inverted 3 times.

Fixation and staining of cells before flow cytometry. Immediately after isolation, the cells were fixed and stained as previously described[41], with some modifications. The cell suspension was centrifuged at 200 × g for 10 min at 4 °C and the supernatant aspirated before fixation for 15 min in 200 µL Fix and Perm® Fixation Buffer A (Invitrogen/Life Technologies, Carlsbad, CA, USA). Cells were washed with 1 mL Stain Buffer (FBS) (BD Biosciences Pharmigen, Franklin Lakes, NJ, USA), centrifuged at 400 × g for 10 min at 4 °C and the supernatant aspirated. This was followed by incubation for 20 min with primary antibody against S100β (monoclonal mouse anti-bovine S100β, 1:250, LifeSpan BioSciences Inc./Nordic BioSite, Täby, Sweden) diluted in 200 µL Fix and Perm® Permeabilization Buffer B (Invitrogen/Life Technologies, Carlsbad, CA, USA). After another wash with Stain Buffer (as above), the cells were incubated for 20 min in the dark with the secondary antibody diluted 1:1000 in 200 µL Fix and Perm® Permeabilization Buffer B (donkey anti-mouse Cy5, Jackson Immunoresearch Laboratories, West Grove, PA, USA). Finally, the cells were washed with Stain Buffer, resuspended in 400 µL of Stain Buffer and transferred to FACS tubes.

Isolation of S100⁺ astrocytes with fluorescence-activated cell sorting. $S100^+$ astrocytes were isolated from the thalamus at 4 months post-CIR using a FACS Aria II equipped with a 100 µm nozzle and DIVA software (BD Biosciences Pharmigen, Franklin Lakes, NJ, USA). Samples were progressively gated based first on size (FSC: forward scatter; size) and granularity (SSC: side scatter; granularity), followed by a pulse geometry gate (FSC-H x FSC-A) where doublets were excluded from the analysis. As controls, amorphous secondary gates were based on cells stained with the secondary antibody only. The cells were sorted with FACS Flow Sheath Fluid (BD Biosciences Pharmigen, Franklin Lakes, NJ, USA) directly into 2 mL sterile micro tubes. Total cell number per sorted population was recorded, resulting in an average of 12,739 ± 746 and 27,630 ± 1,888 astrocytes for controls and irradiated, respectively. Representative data was captured for the first 10,000 cells.

RNA isolation. Immediately after the isolation of cells with FACS, the cell suspension was centrifuged for 20 min at 13,400 rpm, the supernatant was completely aspirated and the cells were frozen at −80 °C until further processed. Total RNA from sorted cells was purified using the RNeasy kit for formalin-fixed paraffin-embedded (FFPE) tissue sections according to the protocol provided by the manufacturer (Qiagen, Hilden, Germany). In order to isolate enough RNA for next generation sequencing, 2–3 animals were pooled into one sample. For controls: 20 animals were pooled into 7 samples, and for irradiated: 12 animals were pooled into 6 samples. Total RNA was eluted in 15 µL RNase-free water and RNA concentrations were measured using a NanoDrop Spectrophotometer (Thermo Scientific, Wilmington, DE, USA).

Next generation sequencing. RNA integrity was assessed using the TapeStation RNA ScreenTape (Agilient Technologies, SantaClara, CA, USA). The samples had low RNA integrity number (RIN) values (between 2-2,7) and were degraded. In the current study we used Illumina's TruSeq® Total Stranded RNA kit with Ribo-Zero (Gold) (Illumina, San Diego, CA, USA) and optimized some of the steps from the standard protocol to achieve an optimal result. TruSeq® Total Stranded RNA kit with Ribo-Zero (Gold) protocol is based on ribosomal RNA depletion and is suitable for degraded RNA samples.

A total of 10 µL (~100 ng) from each sample were used for starting the library preparation. Directly after depletion, a cleanup was performed using 200 uL of the RNAClean XP beads (Beckman Coulter, Brea, CA, USA) for each sample. The fragmentation step was not performed and samples were directly continued to the first strand synthesis of cDNA step. Further, the PCR cycle was increased to 18 cycles for all samples. Libraries were quantified and normalized with Qubit DNA HS Assay kit (Invitrogen/Life Technologies, Carlsbad, CA, USA) and TapeStation (Agilent Technologies, Santa Clara, CA, USA), as recommended by Illumina. The libraries prepared using the same protocol were pooled together. Libraries were sequenced on a NextSeq. 500 with a High output reagent (150 cycles) with a read length of 2 × 75 bp at the Genomics Core Facility, at the Sahlgrenska Academy, University of Gothenburg.

Bioinformatic analysis. The quality of the data was evaluated using Fastqc (http://www.bioinformatics.babraham.ac.uk/projects/fastqc) and the fastq files were filtered using prinseq (version 0.20.3)[60]. Further, the quality filtered fastq files were mapped towards the mouse reference genome (mm10, UCSC assembly, 2011) using STAR (version 2.5.2b)[61]. The resulting alignment was indexed using SAMtools (version 1.3.1)[62]. Moreover, overall mapping quality was examined with qualimap (version 2.2.1)[63] and the gene counts were calculated with HTseq (version 0.5.3p3)[64]. The differential expression was computed using DESeq2[65]. Finally, a pathway analysis was performed on the significantly expressed genes (*P*-value 0.05) with IPA (Ingenuity® Systems, http://www.ingenuity.com/).

Statistical analysis. Cellular quantifications were analyzed using an unpaired Student's t-test, where $p < 0.05$ was considered statistically significant (GraphPad Prism 5.00). All data are shown as mean ± S.E.M. Statistical analysis for NGS is described above.

Data Availability

The datasets generated during and/or analysed during the current study are available from the corresponding author on reasonable request.

References

1. Makale, M. T., McDonald, C. R., Hattangadi-Gluth, J. A. & Kesari, S. Mechanisms of radiotherapy-associated cognitive disability in patients with brain tumours. *Nature reviews. Neurology* **13**, 52–64, https://doi.org/10.1038/nrneurol.2016.185 (2017).
2. Hutchinson, A. D., Pfeiffer, S. M. & Wilson, C. Cancer-related cognitive impairment in children. *Current opinion in supportive and palliative care* **11**, 70–75, https://doi.org/10.1097/spc.0000000000000258 (2017).
3. Hall, P. *et al*. Effect of low doses of ionising radiation in infancy on cognitive function in adulthood: Swedish population based cohort study. *BMJ* **328**, 19, https://doi.org/10.1136/bmj.328.7430.19 (2004).
4. Belka, C., Budach, W., Kortmann, R. D. & Bamberg, M. Radiation induced CNS toxicity–molecular and cellular mechanisms. *Br J Cancer* **85**, 1233–1239, https://doi.org/10.1054/bjoc.2001.2100 (2001).
5. Blomstrand, M. *et al*. Estimated clinical benefit of protecting neurogenesis in the developing brain during radiation therapy for pediatric medulloblastoma. *Neuro-oncology* **14**, 882–889, https://doi.org/10.1093/neuonc/nos120 (2012).
6. Van Someren, E. J. *et al*. Long-term effects of cranial irradiation for childhood malignancy on sleep in adulthood. *European journal of endocrinology* **150**, 503–510 (2004).
7. Moustafa, A. A., McMullan, R. D., Rostron, B., Hewedi, D. H. & Haladjian, H. H. The thalamus as a relay station and gatekeeper: relevance to brain disorders. *Reviews in the neurosciences* **28**, 203–218, https://doi.org/10.1515/revneuro-2016-0067 (2017).
8. Brown, R. E., Basheer, R., McKenna, J. T., Strecker, R. E. & McCarley, R. W. Control of sleep and wakefulness. *Physiological reviews* **92**, 1087–1187, https://doi.org/10.1152/physrev.00032.2011 (2012).
9. Roughton, K., Boström, M., Kalm, M. & Blomgren, K. Irradiation to the young mouse brain impaired white matter growth more in females than in males. *Cell Death Dis* **4**, e897, https://doi.org/10.1038/cddis.2013.423 (2013).
10. Eriksson, Y. *et al*. The anti-asthmatic drug, montelukast, modifies the neurogenic potential in the young healthy and irradiated brain. *Cell Death Dis* **9**, 775, https://doi.org/10.1038/s41419-018-0783-7 (2018).
11. Kalm, M., Lannering, B., Bjork-Eriksson, T. & Blomgren, K. Irradiation-induced loss of microglia in the young brain. *J Neuroimmunol* **206**, 70–75, https://doi.org/10.1016/j.jneuroim.2008.11.002 (2009).
12. Kalm, M., Karlsson, N., Nilsson, M. K. & Blomgren, K. Loss of hippocampal neurogenesis, increased novelty-induced activity, decreased home cage activity, and impaired reversal learning one year after irradiation of the young mouse brain. *Exp Neurol* **247**, 402–409, https://doi.org/10.1016/j.expneurol.2013.01.006 (2013).
13. Neal, M. L., Boyle, A. M., Budge, K. M., Safadi, F. F. & Richardson, J. R. The glycoprotein GPNMB attenuates astrocyte inflammatory responses through the CD44 receptor. *J Neuroinflammation* **15**, 73, https://doi.org/10.1186/s12974-018-1100-1 (2018).
14. Jones, E. V. & Bouvier, D. S. Astrocyte-secreted matricellular proteins in CNS remodelling during development and disease. *Neural plasticity* **2014**, 321209, https://doi.org/10.1155/2014/321209 (2014).
15. Zhao, M., Zhang, T., Yu, F., Guo, L. & Wu, B. E4bp4 regulates carboxylesterase 2 enzymes through repression of the nuclear receptor Rev-erbalpha in mice. *Biochemical pharmacology* **152**, 293–301, https://doi.org/10.1016/j.bcp.2018.04.005 (2018).
16. Anderson, G. D. *et al*. Effect of Traumatic Brain Injury, Erythropoietin, and Anakinra on Hepatic Metabolizing Enzymes and Transporters in an Experimental Rat Model. *The AAPS journal* **17**, 1255–1267, https://doi.org/10.1208/s12248-015-9792-y (2015).
17. Su, E. J. *et al*. Activation of PDGF-CC by tissue plasminogen activator impairs blood-brain barrier integrity during ischemic stroke. *Nat Med* **14**, 731–737, https://doi.org/10.1038/nm1787 (2008).
18. Dinarello, C. A. Immunological and inflammatory functions of the interleukin-1 family. *Annual review of immunology* **27**, 519–550, https://doi.org/10.1146/annurev.immunol.021908.132612 (2009).
19. Yang, J. *et al*. BANK1 alters B cell responses and influences the interactions between B cells and induced T regulatory cells in mice with collagen-induced arthritis. *Arthritis research & therapy* **20**, 9, https://doi.org/10.1186/s13075-017-1503-x (2018).
20. Patel, P. R. *et al*. Increased metabolic rate and insulin sensitivity in male mice lacking the carcino-embryonic antigen-related cell adhesion molecule 2. *Diabetologia* **55**, 763–772, https://doi.org/10.1007/s00125-011-2388-x (2012).
21. Yu, M. H. *et al*. Up-regulated CKS2 promotes tumor progression and predicts a poor prognosis in human colorectal cancer. *American journal of cancer research* **5**, 2708–2718 (2015).
22. Fujimura, H. *et al*. Immunological localization and ontogenetic development of inhibin alpha subunit in rat brain. *J Neuroendocrinol* **11**, 157–163 (1999).
23. Brederlau, A., Faigle, R., Kaplan, P., Odin, P. & Funa, K. Bone morphogenetic proteins but not growth differentiation factors induce dopaminergic differentiation in mesencephalic precursors. *Mol Cell Neurosci* **21**, 367–378 (2002).
24. Zhang, L. *et al*. Small Molecules Efficiently Reprogram Human Astroglial Cells into Functional Neurons. *Cell Stem Cell* **17**, 735–747, https://doi.org/10.1016/j.stem.2015.09.012 (2015).
25. Zhang, Y. *et al*. Methylation-reprogrammed Wnt/beta-catenin signalling mediated prenatal hypoxia-induced brain injury in foetal and offspring rats. *Journal of cellular and molecular medicine*. https://doi.org/10.1111/jcmm.13660 (2018).
26. Li, H. *et al*. The tandem PH domain-containing protein 2 (TAPP2) regulates chemokine-induced cytoskeletal reorganization and malignant B cell migration. *PLoS One* **8**, e57809, https://doi.org/10.1371/journal.pone.0057809 (2013).
27. Neupert, C. *et al*. Regulated Dynamic Trafficking of Neurexins Inside and Outside of Synaptic Terminals. *J Neurosci* **35**, 13629–13647, https://doi.org/10.1523/jneurosci.4041-14.2015 (2015).
28. Fernstrom, E. *et al*. Cerebrospinal fluid markers of extracellular matrix remodelling, synaptic plasticity and neuroinflammation before and after cranial radiotherapy. *Journal of internal medicine*. https://doi.org/10.1111/joim.12763 (2018).
29. Roberts, A. J., Kon, T., Knight, P. J., Sutoh, K. & Burgess, S. A. Functions and mechanics of dynein motor proteins. *Nature reviews. Molecular cell biology* **14**, 713–726, https://doi.org/10.1038/nrm3667 (2013).
30. Huang, R. *et al*. MicroRNA-133b Negatively Regulates Zebrafish Single Mauthner-Cell Axon Regeneration through Targeting tppp3 *in Vivo*. *Frontiers in molecular neuroscience* **10**, 375, https://doi.org/10.3389/fnmol.2017.00375 (2017).
31. Stroud, M. J. *et al*. GAS2-like proteins mediate communication between microtubules and actin through interactions with end-binding proteins. *Journal of cell science* **127**, 2672–2682, https://doi.org/10.1242/jcs.140558 (2014).
32. Schmidt, V. A. *et al*. IQGAP2 functions as a GTP-dependent effector protein in thrombin-induced platelet cytoskeletal reorganization. *Blood* **101**, 3021–3028, https://doi.org/10.1182/blood-2002-09-2807 (2003).
33. Had, L., Faivre-Sarrailh, C., Legrand, C. & Rabie, A. The expression of tropomyosin genes in pure cultures of rat neurons, astrocytes and oligodendrocytes is highly cell-type specific and strongly regulated during development. *Brain research. Molecular brain research* **18**, 77–86 (1993).
34. Hares, K. *et al*. Overexpression of Kinesin Superfamily Motor Proteins in Alzheimer's Disease. *Journal of Alzheimer's disease: JAD* **60**, 1511–1524, https://doi.org/10.3233/jad-170094 (2017).
35. Monje, M. L., Toda, H. & Palmer, T. D. Inflammatory blockade restores adult hippocampal neurogenesis. *Science* **302**, 1760–1765, https://doi.org/10.1126/science.1088417 (2003).
36. Roughton, K., Kalm, M. & Blomgren, K. Sex-dependent differences in behavior and hippocampal neurogenesis after irradiation to the young mouse brain. *Eur J Neurosci* **36**, 2763–2772, https://doi.org/10.1111/j.1460-9568.2012.08197.x (2012).

37. Boström, M., Kalm, M., Karlsson, N., Hellström Erkenstam, N. & Blomgren, K. Irradiation to the young mouse brain caused long-term, progressive depletion of neurogenesis but did not disrupt the neurovascular niche. *J Cereb Blood Flow Metab* **33**, 935–943, https://doi.org/10.1038/jcbfm.2013.34 (2013).
38. Ferguson, B. R. & Gao, W. J. Development of thalamocortical connections between the mediodorsal thalamus and the prefrontal cortex and its implication in cognition. *Frontiers in human neuroscience* **8**, 1027, https://doi.org/10.3389/fnhum.2014.01027 (2014).
39. Hellström, N. A., Björk-Eriksson, T., Blomgren, K. & Kuhn, H. G. Differential recovery of neural stem cells in the subventricular zone and dentate gyrus after ionizing radiation. *Stem Cells* **27**, 634–641, https://doi.org/10.1634/stemcells.2008-0732 (2009).
40. Baumann, N. & Pham-Dinh, D. Biology of oligodendrocyte and myelin in the mammalian central nervous system. *Physiological reviews* **81**, 871–927, https://doi.org/10.1152/physrev.2001.81.2.871 (2001).
41. Hellström, N. A., Zachrisson, O., Kuhn, H. G. & Patrone, C. Rapid Quantification of Neurons and Stem/Progenitor Cells in the Adult Mouse Brain by Flow Cytometry. *Letters in Drug Design and Discovery* **4**, 532–539 (2007).
42. Robbins, M. E., Bourland, J. D., Cline, J. M., Wheeler, K. T. & Deadwyler, S. A. A model for assessing cognitive impairment after fractionated whole-brain irradiation in nonhuman primates. *Radiat Res* **175**, 519–525, https://doi.org/10.1667/rr2497.1 (2011).
43. Greene-Schloesser, D. M. *et al*. Cellular response of the rat brain to single doses of (137)Cs gamma rays does not predict its response to prolonged 'biologically equivalent' fractionated doses. *Int J Radiat Biol* **90**, 790–798, https://doi.org/10.3109/09553002.2014.933915 (2014).
44. Yuan, H. *et al*. Effects of fractionated radiation on the brain vasculature in a murine model: blood-brain barrier permeability, astrocyte proliferation, and ultrastructural changes. *Int J Radiat Oncol Biol Phys* **66**, 860–866, https://doi.org/10.1016/j.ijrobp.2006.06.043 (2006).
45. Gaber, M. W. *et al*. Differences in ICAM-1 and TNF-alpha expression between large single fraction and fractionated irradiation in mouse brain. *Int J Radiat Biol* **79**, 359–366 (2003).
46. Blomstrand, M., Kalm, M., Grander, R., Bjork-Eriksson, T. & Blomgren, K. Different reactions to irradiation in the juvenile and adult hippocampus. *Int J Radiat Biol* **90**, 807–815, https://doi.org/10.3109/09553002.2014.942015 (2014).
47. Monje, M. L., Mizumatsu, S., Fike, J. R. & Palmer, T. D. Irradiation induces neural precursor-cell dysfunction. *Nat Med* **8**, 955–962, https://doi.org/10.1038/nm749 (2002).
48. Fukuda, A. *et al*. Age-dependent sensitivity of the developing brain to irradiation is correlated with the number and vulnerability of progenitor cells. *J Neurochem* **92**, 569–584, https://doi.org/10.1111/j.1471-4159.2004.02894.x (2005).
49. Fike, J. R., Rosi, S. & Limoli, C. L. Neural precursor cells and central nervous system radiation sensitivity. *Semin Radiat Oncol* **19**, 122–132, https://doi.org/10.1016/j.semradonc.2008.12.003 (2009).
50. Zajac-Spychala, O. *et al*. Long-term brain structural magnetic resonance imaging and cognitive functioning in children treated for acute lymphoblastic leukemia with high-dose methotrexate chemotherapy alone or combined with CNS radiotherapy at reduced total dose to 12 Gy. *Neuroradiology* **59**, 147–156, https://doi.org/10.1007/s00234-016-1777-8 (2017).
51. Simo, M. *et al*. Brain damage following prophylactic cranial irradiation in lung cancer survivors. *Brain imaging and behavior* **10**, 283–295, https://doi.org/10.1007/s11682-015-9393-5 (2016).
52. Mabbott, D. J., Noseworthy, M. D., Bouffet, E., Rockel, C. & Laughlin, S. Diffusion tensor imaging of white matter after cranial radiation in children for medulloblastoma: correlation with IQ. *Neuro-oncology* **8**, 244–252, https://doi.org/10.1215/15228517-2006-002 (2006).
53. Greene-Schloesser, D. *et al*. Radiation-induced brain injury: A review. *Frontiers in oncology* **2**, 73, https://doi.org/10.3389/fonc.2012.00073 (2012).
54. Dellani, P. R. *et al*. Late structural alterations of cerebral white matter in long-term survivors of childhood leukemia. *Journal of magnetic resonance imaging: JMRI* **27**, 1250–1255, https://doi.org/10.1002/jmri.21364 (2008).
55. Mulhern, R. K. *et al*. Risks of young age for selected neurocognitive deficits in medulloblastoma are associated with white matter loss. *J Clin Oncol* **19**, 472–479 (2001).
56. Reddick, W. E. *et al*. Subtle white matter volume differences in children treated for medulloblastoma with conventional or reduced dose craniospinal irradiation. *Magnetic resonance imaging* **18**, 787–793 (2000).
57. Naylor, A. S. *et al*. Voluntary running rescues adult hippocampal neurogenesis after irradiation of the young mouse brain. *Proc Natl Acad Sci USA* **105**, 14632–14637, https://doi.org/10.1073/pnas.0711128105 (2008).
58. Rooney, J. W. & Laack, N. N. Pharmacological interventions to treat or prevent neurocognitive decline after brain radiation. *CNS oncology* **2**, 531–541, https://doi.org/10.2217/cns.13.60 (2013).
59. Fowler, J. F. The linear-quadratic formula and progress in fractionated radiotherapy. *Br J Radiol* **62**, 679–694 (1989).
60. Schmieder, R. & Edwards, R. Quality control and preprocessing of metagenomic datasets. *Bioinformatics (Oxford, England)* **27**, 863–864, https://doi.org/10.1093/bioinformatics/btr026 (2011).
61. Dobin, A. *et al*. STAR: ultrafast universal RNA-seq aligner. *Bioinformatics (Oxford, England)* **29**, 15–21, https://doi.org/10.1093/bioinformatics/bts635 (2013).
62. Li, H. *et al*. The Sequence Alignment/Map format and SAMtools. *Bioinformatics (Oxford, England)* **25**, 2078–2079, https://doi.org/10.1093/bioinformatics/btp352 (2009).
63. Okonechnikov, K., Conesa, A. & Garcia-Alcalde, F. Qualimap 2: advanced multi-sample quality control for high-throughput sequencing data. *Bioinformatics (Oxford, England)* **32**, 292–294, https://doi.org/10.1093/bioinformatics/btv566 (2016).
64. Anders, S., Pyl, P. T. & Huber, W. HTSeq–a Python framework to work with high-throughput sequencing data. *Bioinformatics (Oxford, England)* **31**, 166–169, https://doi.org/10.1093/bioinformatics/btu638 (2015).
65. Love, M. I., Huber, W. & Anders, S. Moderated estimation of fold change and dispersion for RNA-seq data with DESeq2. *Genome Biol* **15**, 550, https://doi.org/10.1186/s13059-014-0550-8 (2014).

Acknowledgements

We are grateful for the skillful technical assistance of Rita Grandér and Lindsay Zentveld Einarsson. Further, we thank Professor Carina Mallard for letting us use the gentleMACS Octo Dissociator for the cell dissociation of the thalamus. We thank Elham Rekabdar and Sanna Abrahamsson at the Genomics and Bioinformatics Core Facility platforms, at the Sahlgrenska Academy, University of Gothenburg. This study was supported by grants from the Swedish state under the agreement between the Swedish government and the county councils, the ALF-agreement (ALFGBG-774991, ALFGBG-819811), the Swedish Society of Medicine, the Swedish Childhood Cancer Foundation (Barncancerfonden), the Frimurare Barnhus Foundations of Gothenburg, the Lions Cancer Fund of Western Sweden, the Wilhelm and Martina Lundgren Foundation, the Edith Jacobssons Donation Fund, and Jubileumskliniken's anti-cancer research fund.

Author Contributions

M.K. conceived the overall study and supervised the project. M.B., Y.E. and M.K. designed the experiments. M.B., Y.E. and J.D. conducted the experiments. All of the authors discussed and interpreted the results. M.B., Y.E. and M.K. wrote the manuscript with contributions from all coauthors. J.D. and T.B.-E. revised the manuscript. All authors read and approved the final manuscript.

Additional Information

Supplementary information accompanies this paper at https://doi.org/10.1038/s41598-019-45973-8.

Competing Interests: The authors declare no competing interests.

Publisher's note: Springer Nature remains neutral with regard to jurisdictional claims in published maps and institutional affiliations.